Physics of Plasmas

Benchmarking NIMROD continuum kinetic formulations through the steady-state poloidal flow

Cite as: Phys. Plasmas **28**, 082503 (2021); https://doi.org/10.1063/5.0054978
Submitted: 23 April 2021 . Accepted: 18 July 2021 . Published Online: 03 August 2021

J. R. Jepson, C. C. Hegna, E. D. Held, J. A. Spencer, B. C. Lyons, et al.

Physics of Plasmas ARTICLE scitation.org/journal/php

Benchmarking NIMROD continuum kinetic formulations through the steady-state poloidal flow

Cite as: Phys. Plasmas **28**, 082503 (2021); doi: 10.1063/5.0054978
Submitted: 23 April 2021 · Accepted: 18 July 2021 ·
Published Online: 3 August 2021

View Online Export Citation CrossMark

J. R. Jepson,[1,a] C. C. Hegna,[1,b] E. D. Held,[2,c] J. A. Spencer,[2,d] and B. C. Lyons[3,e]

AFFILIATIONS

[1]Department of Engineering Physics, University of Wisconsin-Madison, Madison, Wisconsin 53706, USA
[2]Department of Physics, Utah State University, Logan, Utah 84322-4415, USA
[3]General Atomics, San Diego, California 92121, USA

[a]Author to whom correspondence should be addressed: jjepson2@wisc.edu
[b]Electronic mail: cchegna@wisc.edu
[c]Electronic mail: eric.held@usu.edu
[d]Electronic mail: andy.spencer@usu.edu
[e]Electronic mail: lyonsbc@fusion.gat.com

ABSTRACT

In this work, continuum kinetic formulations are employed as a mechanism to include closure physics in an extended magnetohydrodynamics model. Two continuum kinetic approaches have been implemented in the plasma fluid code NIMROD [Sovinec *et al.*, "Nonlinear magnetohydrodynamics with high-order finite elements," J. Comput. Phys. **195**, 355 (2004)] including a Chapman–Enskog-like (CEL) formulation and a more conventional δf approach. Ion kinetic closure schemes are employed to describe the neoclassical flow properties in axisymmetric toroidal geometry. In particular, predictions for steady-state values of poloidal flow profiles in tokamak geometry are provided using both the δf formulation and two different solution techniques for the CEL approach. These results are benchmarked against analytic theory predictions as well as results from the drift kinetic code DK4D. The continuum kinetic formulations employed here show agreement with both the analytic theory and DK4D results, and offer a novel velocity space representation involving higher-order finite elements in pitch angle.

I. INTRODUCTION

Fluid-based models are commonly employed to describe macroscopic plasma behavior in toroidal confinement devices. However, many important phenomena require the inclusion of kinetic physics. Important examples of tokamak physics that require the inclusion of kinetic effects include the neoclassical tearing mode[1–7] and the resistive wall mode (RWM).[8–12] For the RWM, the properties of the poloidal and toroidal rotation profiles impact stability predictions.[11,12] Nonlinear field error penetration by resonant magnetic perturbations (RMPs) in tokamaks is also impacted by macroscopic flow dynamics,[13–15] which requires a neoclassical (preferably kinetic) treatment to provide a comprehensive prediction for the flow evolution. In the following, we describe efforts to incorporate important kinetic theory-based physics into extended magnetohydrodynamic (MHD) models using a coupled continuum kinetic approach to describe ion dynamics. In particular, this work concentrates on predictions for poloidal flow profiles in tokamak geometry using continuum kinetic models in NIMROD.[16] These predictions are benchmarked against analytic theory and prior drift-kinetic calculations.[17]

Two continuum drift kinetic models are currently implemented in the plasma fluid code NIMROD: a more conventional δf implementation[18] and a Chapman–Enskog-like (CEL) implementation.[19] The CEL approach[19–21] allows for a tight, self-consistent coupling between the fluid equations and the kinetics by specifying that the number density (n), temperature (T), and flow velocity ($\mathbf{u}$), which are separately evolved by the fluid equations, be contained in the zeroth-order (in $\delta \equiv \rho/L$, where ρ is the Larmor radius and L is a macroscopic length scale) evolving Maxwellian distribution function. The first-order distribution function then has no density, momentum, or temperature moment. Closure quantities in the fluid equations (not n, T, or $\mathbf{u}$) are found by taking appropriate velocity moments of the first-order kinetic distribution function.

In NIMROD, the δf implementation has been sufficiently benchmarked,[16] but the CEL implementation is relatively new. The goal of the CEL implementation is to enable rigorous kinetic closure of NIMROD's fluid model, which is not possible with the conventional δf approach for the simple reason that the n, $\mathbf{u}$, and T moments of the kinetic distortion in this approach are non-zero. This allows the possibilities of inconsistencies developing between those moments of the kinetic distortion and the fluid variables. For these reasons, the conventional δf approach is not suitable for computing bulk closures in extended MHD modeling. Whereas the CEL approach provides consistency in closures for bulk species, the δf approach is still useful for coupling a minority species, like energetic ions, into NIMROD. However, in the present work, we use the δf method as simply another approach in computing the bulk ion poloidal flow offset. Before testing the full fluid/kinetic coupling of the CEL implementation however, we first benchmark the solely kinetic aspects of the formulation. This allows us to test subtle details of the formulation, such as the feasibility of incorporating moments of the kinetic distortion in the kinetic equation in a fully time-implicit fashion, among others. Note a time-implicit approach is used for all the solution methods herein. We demonstrate herein two methods for solving the CEL drift kinetic equation (DKE) in NIMROD. We refer to them as the *DK4D approach* and the *collisional drive approach*. Along with the δf approach, we then have three different ways of kinetically solving for the poloidal flow in NIMROD.

The damping of poloidal flows in tokamaks is fundamentally kinetic in nature. In the banana collisionality regime, it arises from the collisions of "passing" particles (which carry the poloidal flow) with "trapped" particles.[22,23] Examining the poloidal flow profiles provides a simple way to test the kinetic aspects of our implementations. Specifically, we look at the value for the steady-state ion poloidal flow coefficient, α, which is defined as follows:

$$\alpha = -\frac{\mathbf{u}_i \cdot \nabla\theta}{\mathbf{B} \cdot \nabla\theta} \frac{e\langle B^2\rangle}{I(\mathrm{d}T_i/\mathrm{d}\psi)}, \tag{1}$$

where T_i is the ion temperature, $\mathbf{B}$ is the magnetic field, $B = |\mathbf{B}|$, θ is the poloidal angle, e is the elementary charge unit, ψ is the poloidal magnetic flux normalized by 2π, $I(\psi) = RB_\phi$ with R the major radius and B_ϕ the toroidal component of the magnetic field, and brackets represent the flux-surface average defined as

$$\langle f(\psi,\theta)\rangle = \int_0^{2\pi} \frac{f(\psi,\theta)\mathrm{d}\theta}{\mathbf{B}\cdot\nabla\theta} \Big/ \int_0^{2\pi} \frac{\mathrm{d}\theta}{\mathbf{B}\cdot\nabla\theta}. \tag{2}$$

This definition for α is standard in neoclassical theory. For $\nabla \cdot \mathbf{u}_i = 0$ [which will be true in the steady state to $O(\delta)$, see Eqs. (3) and (9) below], the quantity $\mathbf{u}_i \cdot \nabla\theta/\mathbf{B}\cdot\nabla\theta$ (and hence α) can be shown to be a flux function.[22,23] Analytically, the value of α can be obtained using a moment approach, where needed viscosity coefficients are found through a solution of the drift kinetic equation in each asymptotic regime. Details for these calculations are provided in Refs. 22–24. Herein, computational predictions of α are compared against analytic predictions. We also compare our numerical results for α to those from another drift kinetic code, DK4D.[17] DK4D implements a similar CEL drift kinetic equation and allows for code comparison of the axisymmetric, steady-state results presented here.

II. ASSUMPTIONS AND PRELIMINARIES

The axisymmetric equilibrium magnetic field has the form

$$\mathbf{B} = I(\psi)\nabla\phi + \nabla\phi \times \nabla\psi, \tag{3}$$

and, along with the zeroth-order total pressure, satisfies the Grad–Shafranov equation. In this work, the magnetic field is stationary, and the zeroth-order ion pressure, p_{i0}, is exactly half of the zeroth-order total pressure, p_0. For a given equilibrium, we have the freedom to partition p_{i0} between n_{i0} and T_{i0}, allowing us to explore different collisionality regimes. For further details on the equilibria used, see Sec. VI.

NIMROD uses a right-handed (R, Z, ϕ) cylindrical coordinate system in physical space. In velocity space, we use $\xi \equiv v_\parallel/v$ and $s \equiv v/v_{Ti}$, where v is speed, $v_\parallel$ is velocity along the magnetic field, $v_{Ti} = \sqrt{2T_{i0}/m_i}$ is the ion thermal speed, T_{i0} is the zeroth-order ion temperature, and m_i is the ion mass. We assume protons for the ions in this work.

For testing purposes, we restrict ourselves to axisymmetric geometry and quote steady-state values from the simulations when performing the benchmarks. A study of time dependent effects, already implemented in NIMROD, is forth coming.

III. KINETIC CLOSURES IN FLUID EQUATIONS.

We here demonstrate what kinetic closures would look like in the fluid equations for the general case and when evolving all quantities in time. To first-order in δ, the fluid equations for the ions take the form[19]

$$\frac{\partial n_i}{\partial t} + \nabla\cdot(n_i\mathbf{u}_i) = 0 \tag{4}$$

for number density,

$$m_i n_i\left(\frac{\partial \mathbf{u}_i}{\partial t}\right) = -\nabla(n_iT_i) - \nabla\cdot((p_{i\parallel}-p_{i\perp})(\mathbf{bb}-\mathbf{I}/3)) + en_i(\mathbf{E}+\mathbf{u}_i\times\mathbf{B}), \tag{5}$$

for flow velocity, and

$$\frac{3}{2}n_i\left(\frac{\partial T_i}{\partial t} + \mathbf{u}_i\cdot\nabla T_i\right) = -\nabla\cdot\left(q_{i\parallel}\mathbf{b} + \frac{5n_iT_i}{2eB}\mathbf{b}\times\nabla T_i\right) - n_iT_i(\nabla\cdot\mathbf{u}_i), \tag{6}$$

for temperature. Here, $\mathbf{b} = \mathbf{B}/B$, $\mathbf{I}$ is the identity tensor, $\mathbf{E}$ is the electric field, $(p_{i\parallel} - p_{i\perp})$ is the difference between the parallel and perpendicular pressures, and $q_{i\parallel}$ is the parallel heat flux. Note that we employ the ordering $\mathbf{u}_i \sim O(\delta)$ herein, so the convective derivative term is neglected in Eq. (5).

In extended MHD calculations, the total momentum balance equation is often used in place of Eq. (5). Due to quasineutrality, it does not contain a contribution from the electric field. Instead, the ion viscosity,[18,19,25]

$$\Pi_{i1} = (p_{i\parallel} - p_{i\perp})(\mathbf{bb} - \mathbf{I}/3), \tag{7}$$

is critical and dominates the corresponding electron viscosity. It thus provides the dominant kinetic addition to the total momentum balance equation. With an appropriate closure for the electron pressure in the total momentum balance equation, and with an appropriate Ohm's law to govern the time evolution of the magnetic field, what then remains is to close for $(p_{i\parallel} - p_{i\perp})$ and $q_{i\parallel}$ in the fluid equations. In a solely fluid approach, heuristic closures can be used for

$(p_{i\parallel} - p_{i\perp})$ and $q_{i\parallel}$. However, when coupled with kinetics, these quantities can be rigorously specified through $O(\delta)$ as

$$(p_{i\parallel} - p_{i\perp}) = 2\pi m_i v_{Ti}^5 \int_0^\infty \mathrm{d}s s^4 \int_{-1}^1 \mathrm{d}\xi P_2(\xi) f_{i1} \tag{8}$$

and

$$q_{i\parallel} = \pi m_i v_{Ti}^6 \int_0^\infty \mathrm{d}s s^5 \int_{-1}^1 \mathrm{d}\xi P_1(\xi) f_{i1}, \tag{9}$$

where $P_1(\xi)$ and $P_2(\xi)$ are the first and second-order Legendre polynomials in ξ, and f_{i1} is the first-order ion distribution function. Note that the macroscopic flow ($\mathbf{u}_i$) does not appear in Eqs. (8) and (9) because it is ordered as $O(\delta)$.

IV. POLOIDAL FLOW

We define $U_{i\theta} \equiv \mathbf{u}_i \cdot \nabla\theta/\mathbf{B} \cdot \nabla\theta$. $U_{i\theta}$ can be obtained by assuming that the lowest-order perpendicular flow is given by the sum of the diamagnetic and $\mathbf{E} \times \mathbf{B}$ flows, namely,

$$\mathbf{u}_{i1} = \mathbf{u}_{i1\parallel} + \mathbf{u}_{i1\perp} = \frac{u_{i1\parallel}}{B}\mathbf{B} + \left(\frac{p_{i0}'}{e n_{i0}} + \phi_0'\right)\left(\frac{\mathbf{B} \times \nabla\psi}{B^2}\right), \tag{10}$$

from which $U_{i\theta}$ is easily found to be

$$U_{i\theta} = \frac{u_{i1\parallel}}{B} + \frac{I}{B^2}\left(\frac{p_{i0}'}{e n_{i0}} + \phi_0'\right). \tag{11}$$

Here, ϕ_0 is the zeroth-order electric potential, and prime ($'$) signifies $\mathrm{d}/\mathrm{d}\psi$. As is standard in neoclassical theory, the stress tensor contribution to the perpendicular flow (which is one order higher in δ) has been omitted in Eq. (10).

The poloidal flow constant α, which is proportional to $U_{i\theta}$ [see Eq. (1)], depends on both the trapped fraction,

$$f_t = 1 - \frac{3}{4}\langle B^2 \rangle \int_0^{\frac{1}{B_{\max}}} \frac{\lambda \mathrm{d}\lambda}{\langle \sqrt{1 - \lambda B} \rangle}, \tag{12}$$

where $B_{\max}$ is the maximum value for B on a given flux surface and $\lambda \equiv v_\perp^2/(v^2 B)$ (with $v_\perp$ the velocity perpendicular to $\mathbf{B}$), and the collisionality,

$$\nu_i^\star = \frac{e^4 n_{i0} \ln \Lambda_{ii}}{4\pi\epsilon_0^2 m_i^2 v_{Ti}^3 \epsilon^{3/2}} \cdot \left(\frac{qR}{v_{Ti}}\right) \equiv \frac{\hat{\nu}}{\epsilon^{3/2}}. \tag{13}$$

Here, ϵ_0 is the permittivity of free space, ϵ is the inverse aspect ratio, $\ln \Lambda_{ii}$ is the Coulomb logarithm, q is the safety factor ($q = \langle \mathbf{B} \cdot \nabla\phi \rangle / \langle \mathbf{B} \cdot \nabla\theta \rangle$), and $\hat{\nu}$ is defined for consistency with Ref. 17. There are two different analytic results for α that we use in the banana regime ($\nu^\star \ll 1$). Both results are obtained by initially letting[22–24]

$$f_{i1} = -\frac{I s \xi v_{Ti}}{\Omega}\left(\frac{n_{i0}'}{n_{i0}} + \frac{e\phi_0'}{T_{i0}} + (s^2 - 3/2)\frac{T_{i0}'}{T_{i0}}\right) f_{Mi} + g \tag{14}$$

and expanding g in associated Laguerre polynomials $L_k^{(3/2)}(s^2)$ of order 3/2. Here, $\Omega = eB/m_i$ is the gyrofrequency, and $f_{Mi} = \frac{n_{i0}}{v_{Ti}^3 \pi^{3/2}} e^{-s^2}$ is a Maxwellian. Putting this into the δf DKE (see Sec. V A), and taking appropriate velocity moments, leads to a set of coupled equations for the expansion coefficients. The first of these two analytic results in the $\nu^\star \ll 1$ regime is given by Hirshman and Sigmar,[22,23]

$$\alpha_{\mathrm{H-S}} = \frac{-1.173}{1 + 0.462 f_t/(1 - f_t)}. \tag{15}$$

The second is a more refined analytic approach given by Taguchi,[24] where the analytic treatment uses the exact pitch-angle-scattering part of the collision operator and expands the non-pitch-angle-scattering part of the collision operator up to $l = 3$ in Legendre polynomials. This differs from the Hirshman and Sigmar result,[22] who also used the exact pitch-angle-scattering part of the collision operator, but used a model collision operator for the non-pitch-angle-scattering part [proportional to $P_1(\xi)$]. For Taguchi's formula, see Eq. (18) of Ref. 24.

V. KINETIC FORMULATIONS

Here, we discuss the two continuum drift kinetic implementations currently in NIMROD. The first uses the δf kinetic approach, where the distribution function f_{i1} beyond a static lowest-order distribution is solved for, and relevant fluid quantities of interest are obtained by taking appropriate moments. In the second, the CEL implementation, the distribution function strictly contains information needed to close NIMROD's set of fluid equations. We will enumerate the details of, and some important distinctions between, the two approaches in Subsections V A and V B.

A. δf Approach

1. δf Equation

In this work, the $O(\delta)$ δf DKE[18] solved in NIMROD is

$$\frac{\partial f_{i1}}{\partial t} + \xi s v_{Ti} \mathbf{b} \cdot \nabla f_{i1} - \frac{1 - \xi^2}{2\xi}[\xi s v_{Ti} \mathbf{b} \cdot \nabla \ln B]\frac{\partial f_{i1}}{\partial \xi} - C(f_{i1}) = -\frac{e f_{i0}(\mathbf{v}_D \cdot \nabla\psi)}{T_{i0}}\left(\frac{p_{i0}'}{e n_{i0}} + \phi_0'\right) + \left(\frac{5}{2} - s^2\right)\frac{f_{i0}}{T_{i0}}(\mathbf{v}_D \cdot \nabla\psi) T_{i0}', \tag{16}$$

where C is the full, linearized Fokker–Planck Coulomb collision operator, $\mathbf{v}_D = \frac{T_{i0} s^2}{eB}(1 + \xi^2)\mathbf{b} \times \nabla \ln B + \frac{\mu_0 s^2 T_{i0}}{eB^2}[2\xi^2 \mathbf{J}_\perp + (1 - \xi^2)\mathbf{J}_\parallel]$, μ_0 is the permeability of free space, $\mathbf{J}_\perp$ and $\mathbf{J}_\parallel$ are the perpendicular and parallel current densities [$\mathbf{J}_\parallel = (1/\mu_0)\mathbf{b} \cdot \nabla \times \mathbf{B}$, and $\mathbf{J}_\perp = \mathbf{J} - \mathbf{J}_\parallel$], and f_{i0} is the zeroth-order ion distribution function which is a stationary Maxwellian ($f_{i0} = f_{Mi}$). For further details on the collision operator, see the Appendix and Refs. 16 and 26. In deriving this equation, it was assumed that $\mathbf{v}_\parallel \cdot \nabla\phi_1 = 0$, a common assumption in neoclassical transport literature.[22,23]

2. Specification for ϕ_0'

It can be seen from Eq. (16) that the δf approach still requires specification for the electrostatic potential. As we show subsequently though, the choice for ϕ_0' does not affect the result for the steady-state poloidal flow. It will, however, affect the general flow dynamics; thus, there is the need for a specification for ϕ_0'. Although it is not needed for the results in this paper, we briefly summarize the specification method that would be used for general calculations in the δf approach. For our purpose, we use an approach that does not require coupling to an electron evolution equation (or a subsequent Poisson solve).

From the addition of the first-order electron and ion momentum equations, and under the assumption of axisymmetry, we obtain

$$m_i n_{i0}\frac{\partial(Ru_{i1\phi})}{\partial t}+m_e n_{e0}\frac{\partial(Ru_{e1\phi})}{\partial t}=-\sum_{j=i,e}R\hat{\phi}\cdot\nabla\cdot\boldsymbol{\Pi}_{j1}, \tag{17}$$

where we have neglected the presence of any second-order currents, consistent with Grad–Shafranov solutions defining the magnetic field. We then take the flux-surface average of Eq. (17) [noting the form for $\boldsymbol{\Pi}_{j1}$ from Eq. (7)] to obtain

$$m_i n_{i0}\frac{\partial\langle Ru_{i1\phi}\rangle}{\partial t}+m_e n_{e0}\frac{\partial\langle Ru_{e1\phi}\rangle}{\partial t}=0. \tag{18}$$

Assuming that the flux surface-averaged electron flow does not change on too small of a timescale so that we can omit the second term, which is $O(m_e/m_i)$, we obtain

$$m_i n_{i0}\frac{\partial\langle Ru_{i1\phi}\rangle}{\partial t}\approx 0. \tag{19}$$

Equation (19) is similar to the result used in Refs. 27 and 28, but therein the authors used simply that

$$\frac{\partial u_{i1\phi}}{\partial t}=0.$$

Dotting $R\hat{\phi}$ into Eq. (10), and then flux-surface averaging, we obtain the constant

$$\langle Ru_{i1\phi}\rangle=I\left\langle\frac{u_{i1\parallel}}{B}\right\rangle-I^2\left\langle\frac{B_\theta^2}{B^2B_\phi^2}\right\rangle\left(\frac{p_{i0}'}{en_{i0}}+\phi_0'\right), \tag{20}$$

where $B_\theta\equiv\mathbf{B}\cdot\nabla\theta/|\nabla\theta|$. Choosing $\langle Ru_{i1\phi}\rangle$ is equivalent to choosing the initial perpendicular flow. A simple choice is $\langle Ru_{i1\phi}\rangle=I\langle u_{i1\parallel}/B\rangle_{t=0}$, which is equivalent to specifying that the initial perpendicular flow is zero. With this choice, we obtain

$$\phi_0'=\frac{\left\langle\frac{u_{i1\parallel}}{B}\right\rangle-\left\langle\frac{u_{i1\parallel}}{B}\right\rangle_{t=0}}{I\left\langle\frac{B_\theta^2}{B^2B_\phi^2}\right\rangle}-\frac{p_{i0}'}{en_{i0}}, \tag{21}$$

and therefore we have a specification for ϕ_0' to use in Eq. (16).

3. Solution methodology

Major details of the continuum δf implementation are contained in Ref. 16. To obtain the first-order parallel ion flow from f_{i1}, we use the formula

$$u_{i1\parallel}=\frac{1}{n_{i0}}\int d^3v v_\parallel f_{i1}=\frac{2\pi v_{Ti}^4}{n_{i0}}\int_0^\infty ds s^3\int_{-1}^1 d\xi P_1(\xi)f_{i1}. \tag{22}$$

This equation is nothing more than the definition of the appropriate moment needed to obtain the parallel flow.

To get $U_{i\theta}$ from the ion distribution function, we here show that the specification of ϕ_0' does not affect the result for the steady-state poloidal flow. We first substitute Eq. (14) into Eq. (22). From Eq. (11), one can see that only g will contribute to the poloidal flow. Then, upon substituting the ansatz [Eq. (14)] into the steady-state version of Eq. (16), we find that ϕ_0' cancels out of the equation. So the steady-state equation for g does not depend on ϕ_0', and therefore the steady-state poloidal flow does not depend on the specification of ϕ_0'. For convenience, we set $\phi_0'=-p_{i0}'/(en_{i0})$ (having the $\mathbf{E}\times\mathbf{B}$ flow exactly cancel the diamagnetic flow). From the result of Eq. (11), this then immediately gives that $U_{i\theta}=u_{i1\parallel}/B$, which indicates how to get $U_{i\theta}$ from f_{i1}. Note, this formula for $U_{i\theta}$ only applies because of our choice of ϕ_0'. Once $U_{i\theta}$ is obtained, α is easily obtained from Eq. (1).

B. Chapman–Enskog-like (CEL) Approach

There are a few key differences between the CEL and the conventional δf approach. The first is that the lowest-order distribution function in the CEL method is a flow-shifted Maxwellian, defined in terms of the total number density, temperature, and flow-velocity (as opposed to just the zeroth-order equilibrium values). In the full CEL approach, these fluid quantities are then evolved using the fluid equations. One consequence of this is that the first-order distribution function must satisfy the constraints, $\int d^3v f_{i1}=\int d^3v\mathbf{v}f_{i1}=\int d^3vv^2f_{i1}=0$. These constraints are enforced by the kinetic equation (as can be seen by taking appropriate velocity moments of the DKE).[29] In order to monitor error in the numerics, however, we compute the n_i, $\mathbf{u}_i$, and T_i moments of f_{i1} as a diagnostic in NIMROD. Convergence studies indicate that the magnitude of these moments decrease as resolution is added, thus preserving the analytic properties of the CEL formulation. For the CEL-DKE used here, the velocity is also defined in the macroscopic flow reference frame.[19]

1. CEL Equation

In this section, we state the CEL-DKE to first-order in $\delta_i\equiv\rho_i/L$, which is sufficient for processes that evolve on the diamagnetic drift timescale or faster.[19,29] The full O(δ_i) CEL-DKE is currently coded in NIMROD. However, with our assumptions of an axisymmetric configuration, and assuming n_i and T_i are stationary flux functions, the CEL-DKE for the ions simplifies to

$$\begin{aligned}&\frac{\partial f_{i1}}{\partial t}+\xi sv_{Ti}\mathbf{b}\cdot\nabla f_{i1}-\frac{1-\xi^2}{2\xi}[\xi sv_{Ti}\mathbf{b}\cdot\nabla\ln B]\frac{\partial f_{i1}}{\partial\xi}-C(f_{i1})\\&=\left\{\frac{\xi sv_{Ti}}{n_iT_i}\left[\frac{2}{3}\mathbf{b}\cdot\nabla(p_{i\parallel}-p_{i\perp})-(p_{i\parallel}-p_{i\perp})\mathbf{b}\cdot\nabla\ln B\right]\right.\\&\quad+P_2(\xi)\frac{2}{3}s^2(\nabla\cdot\mathbf{u}_i-3\mathbf{b}\cdot[\mathbf{b}\cdot\nabla\mathbf{u}_i])+\frac{2}{3n_iT_i}\left(s^2-\frac{3}{2}\right)\nabla\cdot(q_{i\parallel}\mathbf{b})\\&\quad\left.+\frac{I}{3eB}\left[\frac{1}{2}P_2(\xi)2s^2(2s^2-5)+4s^4-20s^2+15\right]\mathbf{b}\cdot\nabla\ln B\frac{dT_i}{d\psi}\right\}f_{Mi},\end{aligned} \tag{23}$$

where v_{Ti} and f_{Mi} are now defined with the full number density and temperature, n_i and T_i. Further simplification occurs by assuming that the ion flow equals the neoclassical value, $\mathbf{u}_i=U_{i\theta}\mathbf{B}-R^2\nabla\phi(p_i'/(en_i)+\phi_0')$ and that the ion parallel heat flux equals the Pfirsch–Schluter-like return component, $\nabla\cdot(q_{i\parallel}\mathbf{b})=-\nabla\cdot\left(\frac{5n_iT_i}{2eB}\mathbf{b}\times\nabla T_i\right)$. The heat flux assumption is required for consistency when not evolving temperature[17] [see Eq. (6)]. With these two assumptions, the CEL-DKE becomes

$$\frac{\partial f_{i1}}{\partial t}+\xi s v_{Ti}\mathbf{b}\cdot\nabla f_{i1}-\frac{1-\xi^2}{2\xi}[\xi s v_{Ti}\mathbf{b}\cdot\nabla\ln B]\frac{\partial f_{i1}}{\partial\xi}-C(f_{i1})$$
$$=\left\{\frac{\xi s v_{Ti}}{n_i T_i}\left[\frac{2}{3}\mathbf{b}\cdot\nabla(p_{i\parallel}-p_{i\perp})-(p_{i\parallel}-p_{i\perp})\mathbf{b}\cdot\nabla\ln B\right]\right.$$
$$-2P_2(\xi)s^2U_{i\theta}\mathbf{b}\cdot\nabla B$$
$$\left.+\frac{2I}{3eB}\left[(P_2(\xi)+2)s^2\left(s^2-\frac{5}{2}\right)\right]\mathbf{b}\cdot\nabla\ln B\frac{dT_i}{d\psi}\right\}f_{Mi}\,. \quad (24)$$

2. Solution methodology I—DK4D approach

For this solution approach, we follow the method that is used in the DK4D code.[17] Because Eq. (24) is linear, it can be solved separately for each of the two non-moment drive terms. The sum satisfies Eq. (24) and can be written

$$f_{i1}=f_{i1,U_{i\theta}}+f_{i1,T_i'}=g_{U_{i\theta}}U_{i\theta}+g_{T_i'}(IT_i'/e), \quad (25)$$

where $f_{i1,U_{i\theta}}$ is the solution with only the $U_{i\theta}$ drive term in Eq. (24), and $f_{i1,T_i'}$ is the solution with only the T_i' drive term in Eq. (24). For convenience, we also define $g_{U_{i\theta}}\equiv f_{i1,U_{i\theta}}/U_{i\theta}$ and $g_{T_i'}\equiv f_{i1,T_i'}/(IT_i'/e)$. Two versions of Eq. (24), one for each of the non-moment drives on the right-hand side, are evolved in time, namely,

$$\mathcal{L}(g_{U_{i\theta}})=\left\{\frac{\xi s v_{Ti}}{n_i T_i}\left[\frac{2}{3}\mathbf{b}\cdot\nabla(p_{i\parallel}-p_{i\perp})|_{g_{U_{i\theta}}}-(p_{i\parallel}-p_{i\perp})|_{g_{U_{i\theta}}}\mathbf{b}\cdot\nabla\ln B\right]\right.$$
$$\left.-2P_2(\xi)s^2\mathbf{b}\cdot\nabla B\right\}f_{Mi}, \quad (26)$$

for $g_{U_{i\theta}}$, where $\mathcal{L}$ represents the linear operator on the LHS of Eq. (24) and

$$(p_{i\parallel}-p_{i\perp})|_{g_{U_{i\theta}}}=2\pi m_i v_{Ti}^5\int_0^\infty \mathrm{d}s s^4\int_{-1}^1 \mathrm{d}\xi P_2(\xi)g_{U_{i\theta}} \quad (27)$$

and

$$\mathcal{L}(g_{T_i'})=\left\{\frac{\xi s v_{Ti}}{n_i T_i}\left[\frac{2}{3}\mathbf{b}\cdot\nabla(p_{i\parallel}-p_{i\perp})|_{g_{T_i'}}-(p_{i\parallel}-p_{i\perp})|_{g_{T_i'}}\mathbf{b}\cdot\nabla\ln B\right]\right.$$
$$\left.+\frac{2}{3B}\left[(P_2(\xi)+2)s^2\left(s^2-\frac{5}{2}\right)\right]\mathbf{b}\cdot\nabla\ln B\right\}f_{Mi}, \quad (28)$$

for $g_{T_i'}$, where

$$(p_{i\parallel}-p_{i\perp})|_{g_{T_i'}}=2\pi m_i v_{Ti}^5\int_0^\infty \mathrm{d}s s^4\int_{-1}^1 \mathrm{d}\xi P_2(\xi)g_{T_i'}. \quad (29)$$

The full solution to Eq. (24) is then given by Eq. (25). Then using the fact that $\langle(p_{i\parallel}-p_{i\perp})\mathbf{b}\cdot\nabla B\rangle=0$ in the steady state (when neglecting ion–electron collisions), and evaluating the $(p_{i\parallel}-p_{i\perp})$ moment with the full f_{i1} from Eq. (25), we obtain

$$U_{i\theta}\langle(p_{i\parallel}-p_{i\perp})|_{g_{U_{i\theta}}}\mathbf{b}\cdot\nabla B\rangle+(IT_i'/e)\langle(p_{i\parallel}-p_{i\perp})|_{g_{T_i'}}\mathbf{b}\cdot\nabla B\rangle=0. \quad (30)$$

This then gives $U_{i\theta}$ as

$$U_{i\theta}=\frac{-(IT_i'/e)\langle(p_{i\parallel}-p_{i\perp})|_{g_{T_i'}}\mathbf{b}\cdot\nabla B\rangle}{\langle(p_{i\parallel}-p_{i\perp})|_{g_{U_{i\theta}}}\mathbf{b}\cdot\nabla B\rangle}, \quad (31)$$

and α is immediately found from Eq. (1). As can be seen from Eqs. (27), (29), and (31), this method uses a ratio of appropriate $P_2(\xi)$ velocity moments of the solution, which provides a contrast with the next approach which will ultimately use an appropriate $P_1(\xi)$ velocity moment of the solution.

3. Solution methodology II—Collisional drive approach

There is a second solution methodology that can be used to find the steady-state $U_{i\theta}$ from the CEL-DKE. This approach involves the particular solution to the steady-state version of Eq. (23). When neglecting collisions, the particular solution is[19]

$$f_{i1,p}=\left[\frac{1}{n_i T_i}\int \mathrm{d}l_\parallel\left(\frac{2}{3}\mathbf{b}\cdot\nabla(p_{i\parallel}-p_{i\perp})\,(p_{i\parallel}-p_{i\perp})\mathbf{b}\cdot\nabla\ln B\right)\right.$$
$$\left.-\left(\frac{m_i U_{i\theta}B}{T_i}+\frac{m_i I}{eBT_i}\left(s^2-\frac{5}{2}\right)T_i'\right)\xi s v_{Ti}\right]f_{Mi}\,, \quad (32)$$

where $l_\parallel$ is length along the magnetic field. We can define the full solution as $f_{i1}=f_{i1,p}+h_i$. Putting this into Eq. (24), we obtain an equation for h_i,

$$\xi s v_{Ti}\mathbf{b}\cdot\nabla h_i-\frac{1-\xi^2}{2\xi}[\xi s v_{Ti}\mathbf{b}\cdot\nabla\ln B]\frac{\partial h_i}{\partial\xi}-C(h_i)$$
$$=\left(\nu_i 2^{3/2}\right)\frac{2^{1/2}}{s^2 v_{Ti}}\frac{IT_i'}{eB}\xi\left[(2s^2-5)\phi_{\mathrm{err}}(s)+5s\frac{d\phi_{\mathrm{err}}(s)}{ds}\right]f_{Mi}\,, \quad (33)$$

where $\phi_{\mathrm{err}}(s)\equiv\left(2/\sqrt{\pi}\right)\int_0^s \mathrm{d}u e^{-u^2}$ is the error function. Solving for h_i (see Sec. VII for a summary of the computational methods used herein) and using the fact that $\int \mathrm{d}^3 v\mathbf{v}f_{i1}=0$ for the CEL approach leads to

$$U_{i\theta}=\frac{1}{n_i B}\int \mathrm{d}^3 v\xi s v_{Ti}h_i, \quad (34)$$

and again α is easily obtained from Eq. (1). An interesting observation is that the moment required to obtain $U_{i\theta}$ from the solution here is identical to the moment required in the conventional δf approach although the drive terms are different.

To summarize, in the interest of vetting the kinetic aspects of the δf and CEL implementations in NIMROD, we have represented three different methods for obtaining α. With the δf implementation, we can obtain α through the parallel flow moment of f_{i1}. With the CEL implementation, we can obtain α through either the DK4D approach or the collisional drive approach. The DK4D approach involves a ratio of quantities that depend on the $P_2(\xi)$ moments of $g_{U_{i\theta}}$ and $g_{T_i'}$, and the collisional drive approach involves a parallel flow moment of h_i.

VI. EQUILIBRIA DETAILS

For this verification exercise, we use the same two JSOLVER[30] Grad–Shafranov equilibria studied in Ref. 17. The first is a high aspect ratio equilibrium with $\epsilon\equiv r/R_0=0.1$ [see Fig. 1(a)], and the second is an NSTX equilibrium [see Fig. 1(b)]. Here, $\bar{\psi}\equiv(\psi-\psi_{\mathrm{axis}})/(\psi_{\mathrm{edge}}-\psi_{\mathrm{axis}})$ is a normalized poloidal flux variable that varies from 0

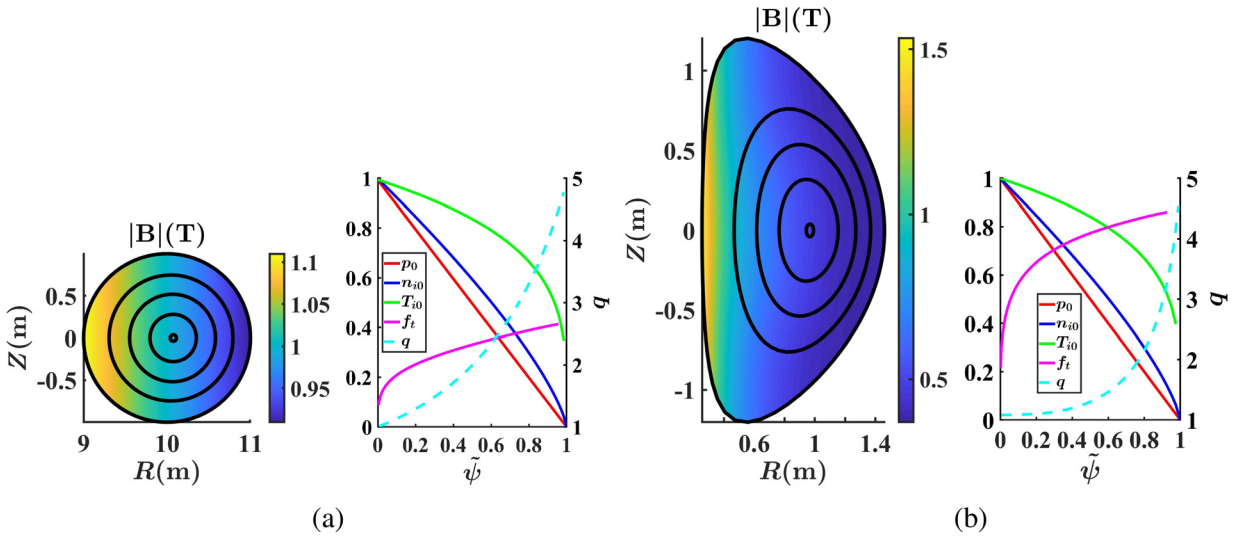

FIG. 1. We use both a high aspect ratio (a) and an NSTX (b) equilibrium. p_0 on axis $\sim 8.0 \times 10^2$ Pa in (a) and $\sim 2.3 \times 10^4$ Pa in (b). In each subfigure, the normalized profiles, safety factor, and f_t are shown at the right, and flux surfaces and $|\mathbf{B}|$ contours are shown at the left. Note the high $|\mathbf{B}|$ variation and high f_t for the NSTX equilibrium.

at the magnetic axis to 1 at the last closed flux surface. We note that for the equilibria herein, f_t is a monotonically increasing function of $\tilde{\psi}$. The high aspect ratio equilibrium easily enables comparison with analytics, whereas the NSTX equilibrium is a more realistic equilibrium with high $|\mathbf{B}|$ variation and high f_t. We specify that the ion number density has the profile $n_{i0} = n_{\text{axis}}(1-\tilde{\psi})^{0.75}$. For each equilibrium, we vary the on-axis ion number density (n_{axis}) to explore different collisionality regimes, leaving p_{i0}, and hence the Grad–Shafranov force balance, fixed.

VII. COMPUTATIONAL METHODS

We will use Eq. (16) with $\phi_0' = -p_{i0}'/(en_{i0})$ to illustrate how the time-stepping scheme works. As in Ref. 16, we step all f_{i1} terms using a Θ-centered implicit approach as follows:

$$\gamma\Delta f_{i1} + \Delta t\Theta\xi s v_{Ti}\mathbf{b}\cdot\nabla(\Delta f_{i1}) - \Delta t\Theta\frac{1-\xi^2}{2\xi}[\xi s v_{Ti}\mathbf{b}\cdot\nabla\ln B]\frac{\partial(\Delta f_{i1})}{\partial\xi} - \Delta t\Theta C(\Delta f_{i1}) = -\Delta t\xi s v_{Ti}\mathbf{b}\cdot\nabla f_{i1}^{k-1} + \Delta t\frac{1-\xi^2}{2\xi}[\xi s v_{Ti}\mathbf{b}\cdot\nabla\ln B]\frac{\partial f_{i1}^{k-1}}{\partial\xi} + \Delta t C(f_{i1}^{k-1}) + \Delta t\left(\frac{5}{2}-s^2\right)\frac{f_{i0}}{T_{i0}}(\mathbf{v}_D\cdot\nabla\psi)T_{i0}', \tag{35}$$

where the superscript on f_{i1} refers to the time step, $\Delta f_{i1} = f_{i1}^k - f_{i1}^{k-1}$, Θ will be set to one for all our cases, and γ is a numerical term that is either 0 or 1 (depending on whether one wants to step directly to the steady-state solution or not). At each time step, we solve for Δf_{i1}, which we then add to f_{i1}^{k-1} to get f_{i1}^k.

NIMROD uses a finite element (FE) representation in its poloidal domain and a Fourier expansion in its toroidal direction. For more details on this representation, see Ref. 31. Although the 3D terms in Eqs. (16) and (23), and subsequent equations are implemented in NIMROD, we only evolve the lowest-order (axisymmetric) Fourier component herein.

In the s dimension, we use a collocation approach, where we evaluate the kinetic equation at a set of collocation points in s. We also use a set of orthogonal polynomials[32] in s to expand the s-derivative terms in the collision operator. In the ξ dimension, we use either Legendre polynomials or 1D finite element (FE) basis functions. For more details on the s and ξ representations, see Sec. VII A and Refs. 16 and 26.

Once our basis is chosen, we follow the Galerkin approach by multiplying the differential equation by the same set of basis functions and then integrating to obtain a matrix equation. For further details, see Refs. 31 and 16. This matrix equation is then solved in NIMROD for the change in the coefficients of the distribution function over the time step. For details on the numerical implementation of the full linearized Fokker–Planck Coulomb collision operator, see the Appendix and Refs. 16 and 26.

A. Further details on ξ representation

In this work, we generalize the 1D FE method from Ref. 16. For finite elements in ξ, we define a logical variable η such that it varies from 0 to the total number of cells as ξ varies from -1 to 1. The mapping from η to ξ allows the velocity grid to vary depending on the position in physical space, allowing the cell boundaries in ξ to vary. This allows one to have cell boundaries in ξ that follow either approximately or exactly the trapped-passing boundary (tpb), which is crucial for convergence in ξ when running in the banana collisionality regime.

We define m_η as the total number of FE cells, $m_{\eta p}$ as the number of cells in the positive passing domain (which mirrors the number in the negative passing domain), and $m_{\eta t}$ as the number of cells in the trapped domain. Then the mapping from η to ξ is given as

$$\xi = \begin{cases} -\cos\left(\dfrac{\theta_{tp}\eta}{m_{\eta p}}\right), & 0 \le \eta < m_{\eta p} \\ -\cos\left(\theta_{tp} + (\pi - 2\theta_{tp})\dfrac{\eta - m_{\eta p}}{m_{\eta t}}\right), & m_{\eta p} \le \eta < m_{\eta p} + m_{\eta t} \\ \cos\left(\dfrac{\theta_{tp}(\eta - m_\eta)}{m_{\eta p}}\right), & m_{\eta p} + m_{\eta t} \le \eta \le m_\eta, \end{cases} \tag{36}$$

where θ_{tp} defines the spacing of the vertex nodes (cell boundaries) in ξ. For uniform grid spacing in pitch angle [i.e., in $\cos^{-1}(\xi)$], $\theta_{tp} \equiv (\pi m_{\eta p})/m_\eta$. To have the grid spacing be constant on flux surfaces but to have the cell boundaries agree with the tpb on the outboard midplane, $\theta_{tp} = \cos^{-1}\left(\sqrt{1 - B_{\min}/B_{\max}}\right)$. We call this an approximate tpb grid. For exact tpb grids, $\theta_{tp} = \cos^{-1}\left(\sqrt{1 - B/B_{\max}}\right)$, where $B(R, Z)$ is the local $|\mathbf{B}|$. To prevent a trapped domain of zero width on the inboard midplane for exact tpb grids, we set

$$\theta_{tp} = \begin{cases} \cos^{-1}\left(\sqrt{1 - B/B_{\max}}\right), & \sqrt{1 - B/B_{\max}} > \delta_{\min}, \\ \cos^{-1}(\delta_{\min}), & \sqrt{1 - B/B_{\max}} \le \delta_{\min}, \end{cases} \tag{37}$$

where $\delta_{\min}$ is some small number ($\delta_{\min} \lesssim 0.01$). For an illustration of the exact tpb grid, see Fig. 2.

When using 1D finite elements (in the η coordinate), we use either Lagrange polynomials with internal nodes uniformly spaced in η or Gauss–Lobatto–Legendre (GLL) polynomials with internal nodes non-uniformly spaced in η. The GLL set gives a natural packing around the tpb (see Fig. 2).

No matter the representation used for ξ, we expand the distribution function as

$$f^k_{i1}(R, Z, \phi, \xi(\eta, R, Z), s_m) = \sum_j f^k_{i1,j,n=0}(\eta, s_m)\alpha_j(R, Z), \tag{38}$$

where $n = 0$ signifies the lowest order Fourier component, $\alpha_j(R, Z)$ are the 2D poloidal FE basis functions, s_m is a specified speed point, and

$$f^k_{i1,j,n=0}(\eta, s_m) = \sum_l f^k_{i1,j,l,m,n=0} Q_l(\eta), \tag{39}$$

where $f^k_{i1,j,l,m,n=0}$ are the coefficients of the distribution function that are advanced in time, and $Q_l(\eta)$ are either the Legendre polynomials, $Q_l(\eta) = P_l(\xi)$, or the 1D FE basis functions [using the mapping in Eq. (36)]. Details on the collocation approach in speed may be found in Refs. 16 and 26. We also note here that many drift kinetic codes, including DK4D,[17] NEO,[33] and CQL3D,[34] use a Legendre polynomial expansion for their pitch angle variable.

The only other subtlety is that, when expanding the distribution function in η, there is an additional term that appears in the DKE. Specifically, we have by the chain rule that

$$\mathbf{b} \cdot \nabla|_\xi f_{i1} \to \mathbf{b} \cdot \nabla|_\eta f_{i1} + \frac{\partial f_{i1}}{\partial \eta}\mathbf{b} \cdot \nabla\eta, \tag{40}$$

where $\eta = \eta(\xi, R, Z)$ is the inverse of the mapping in Eq. (36). For general cases, this extra term is non-zero for velocity grids that vary in the poloidal plane.

Figures 3 and 4 show that for similar degrees of freedom (dof) in ξ, at $\nu^\star \sim 10^{-2}$, convergence in the result for the poloidal flow coefficient α is obtained for the exact tpb FE grid in ξ, but not when using Legendre polynomials in ξ. Physically, this phenomnon is due to the development of a discontinuity in the ξ derivative of f_{i1} in the steady-state banana regime solution at the tpb[22] (see Fig. 5). While velocity grids that follow the exact tpb in velocity space have been used before,[34–36] to our knowledge, this is the first time they have been used with a higher order FE basis of GLL polynomials in pitch angle in a code that can simulate the whole physical domain.

VIII. NUMERICAL RESULTS AND DISCUSSION

Here, we show our numerical results for α and compare with analytics and to results from DK4D.[17] As a reminder, in NIMROD,

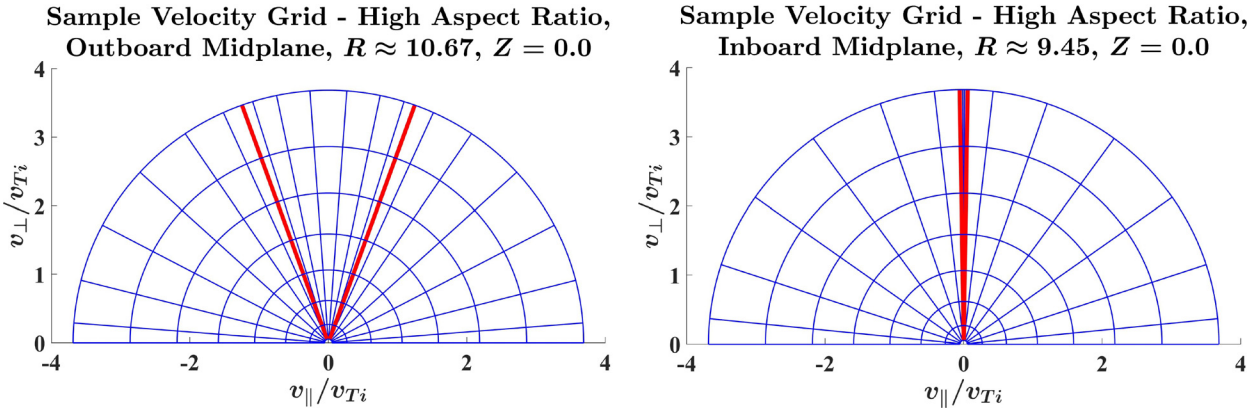

FIG. 2. Sample exact tpb FE grids on both the outboard and inboard midplanes, with three cells in η ($m_\eta = 3$), and $m_{\eta p} = m_{\eta t} = 1$. On the left, the cell boundaries correspond to the tpb and are highlighted in red. On the right, the cell boundaries correspond only approximately to the tpb, with $\delta_{\min} \approx 0.016$. The sample grids here use 8 s points and GLL polynomials in each cell of degree 7. We note the natural packing of the GLL nodes at the tpb.

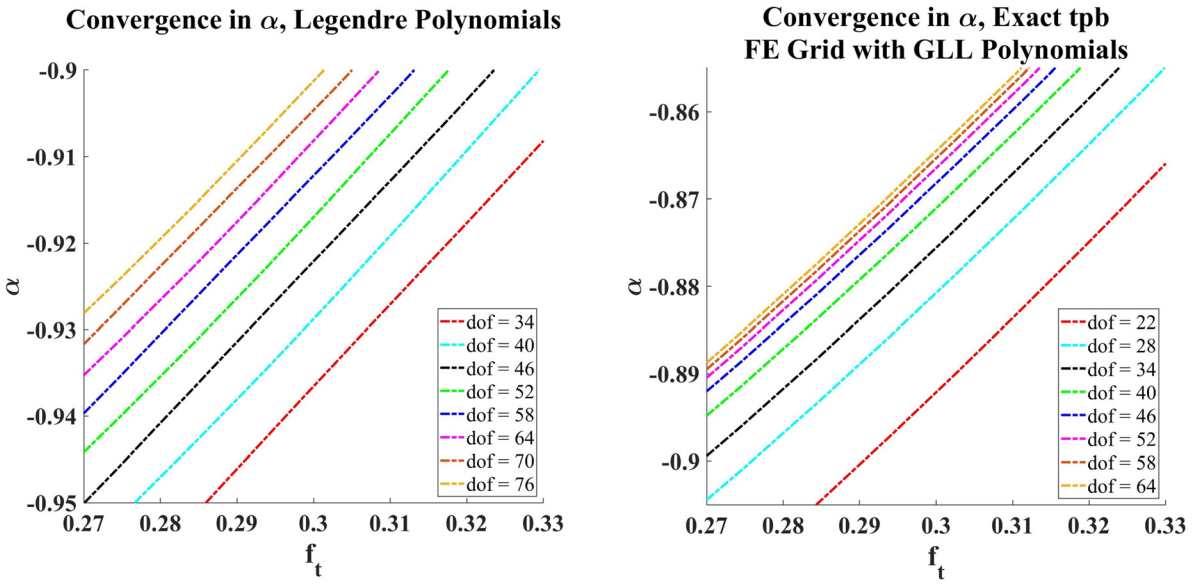

(a) Legendre polynomials in ξ. (b) Exact tpb FE grid in ξ.

FIG. 3. Convergence in α, for the high aspect ratio ($\epsilon = 0.1$) case with $n_{axis} = 5.0 \times 10^{17} m^{-3}$ ($\nu^\star \sim 10^{-2}$). As can be seen on the left (a), 75° of freedom (dof) in ξ is still insufficient for convergence in α when using Legendre polynomials. On the right (b), we can see that convergence in α is essentially obtained at only 58 dof in ξ when using the exact tpb FE grid.

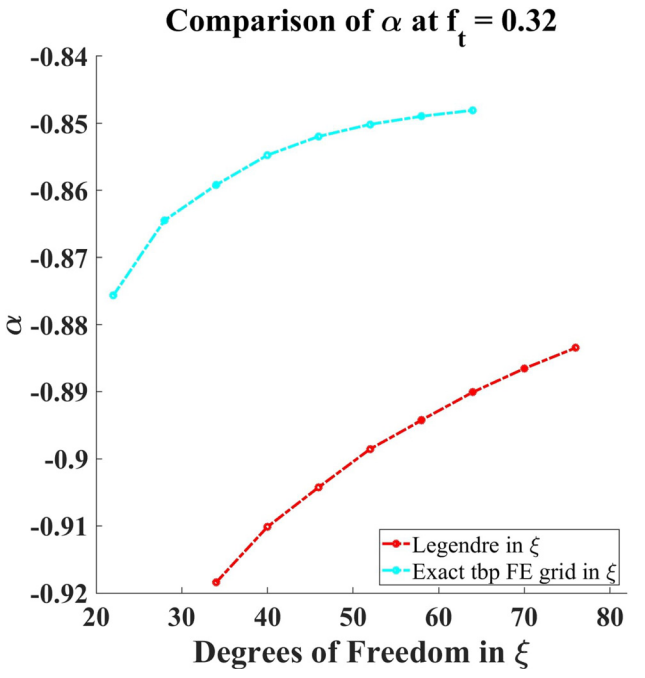

FIG. 4. The superior convergence of the exact tpb FE grid is shown above for the high aspect ratio case ($\epsilon = 0.1$) with $\nu^\star \sim 10^{-2}$. Data taken from Fig. 3 at $f_t \approx 0.32$.

we can calculate α using either the DK4D approach, the collisional drive approach, or the conventional δf approach. Each of these approaches can use various methods of numerical expansion for ξ, as stated in Sec. VII A. For the results herein, we compare two of these methods: an exact tpb FE grid with GLL basis polynomials and Legendre polynomials. Figures 6 and 7 show our α profiles for the high aspect ratio equilibrium at both a higher collisionality ($\hat{\nu} \sim 1$, $n_{axis} = 1.0 \times 10^{19}\, m^{-3}$) and a banana regime collisionality ($\hat{\nu} \sim 10^{-4}$, $n_{axis} = 5.0 \times 10^{17}\, m^{-3}$), respectively. Figures 8 and 9 show our α profiles for the NSTX equilibrium at both a higher collisionality ($\hat{\nu} \sim 1$, $n_{axis} = 2.0 \times 10^{20}\, m^{-3}$) and a banana regime collisionality ($\hat{\nu} \sim 10^{-4}$, $n_{axis} = 1.0 \times 10^{19}\, m^{-3}$), respectively. We plot α vs f_t, which is a flux label for the equilibria used herein (see Fig. 1).

As can be seen from Figs. 6 and 8, excellent agreement is obtained between all of NIMROD's approaches and DK4D in the regime of higher collisionality ($\hat{\nu} \sim 1$). At higher collisionality, details of the collision operator are paramount, and so the high level of agreement in this regime is an excellent result. In Fig. 6, we also plot the plateau regime analytic result from Ref. 22. Differences can be seen between the numerical results and the plateau analytic result. However, the analytic result uses a model collision operator as well as other approximations.[22] In addition, at a $\hat{\nu}$ of about 1, we are at the edge of the plateau regime, rather than squarely inside it. The fact then that the analytic result is as close to the numerical results as it is (within about 8%) is encouraging.

In Figs. 7 and 9, all of NIMROD's Legendre approaches agree with each other, and all of NIMROD's FE approaches agree with each other. We also see some discrepancies between NIMROD's

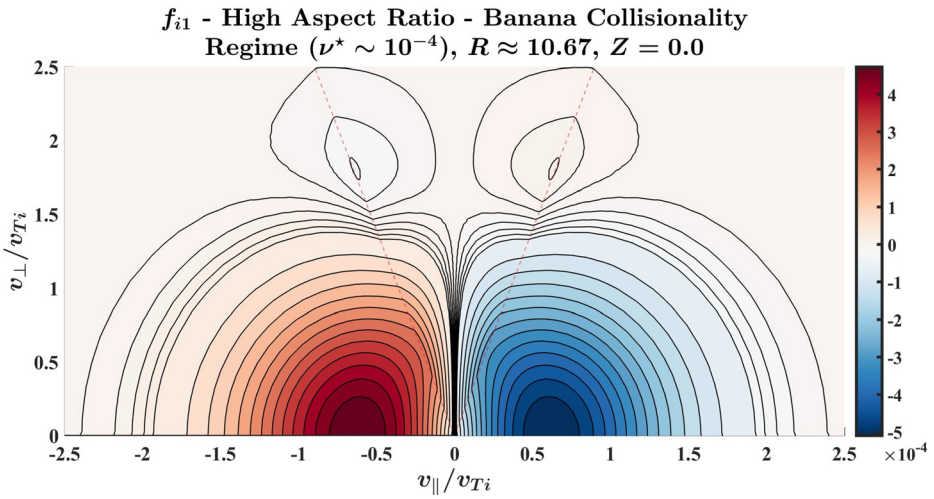

FIG. 5. A contour plot of f_{i1} in velocity space at $R \approx 10.67$, $Z = 0.0$, and $\nu^\star \sim 10^{-4}$. Sharp variation in $\partial f_{i1}/\partial \xi$ at the tpb (shown in red) is easily resolved by the exact tpb FE grid with GLL polynomials.

approaches, analytics, and DK4D. However, we again note here that the Legendre polynomial in ξ cases is not converged at this low collisionality. Obtaining convergence in the banana collisionality regime is difficult with a Legendre basis, as we showed in Fig. 3(a). This occurs because of the discontinuity of the ξ derivative of f_{i1} at the tpb. For these cases, we simply went to the same maximum Legendre degree as DK4D to enable comparison. Through looking at our simulations (see Fig. 4), we have a reason to believe that with increasing Legendre degree, NIMROD's Legendre in ξ results will agree with the exact tpb FE results. However, at the high Legendre degree required for convergence in ξ, memory requirements impose constraints which make these runs too computationally expensive to continue further.

We also note here that Figs. 7 and 9 do not include NIMROD's DK4D approach for the exact tpb FE grid. This is because in the banana collisionality regime, when using the exact tpb FE grid, NIMROD's implementation of the DK4D approach develops a numerical instability involving cell to cell oscillations in physical space that washes out any attempt at a sensible solution. An *ad hoc* diffusion

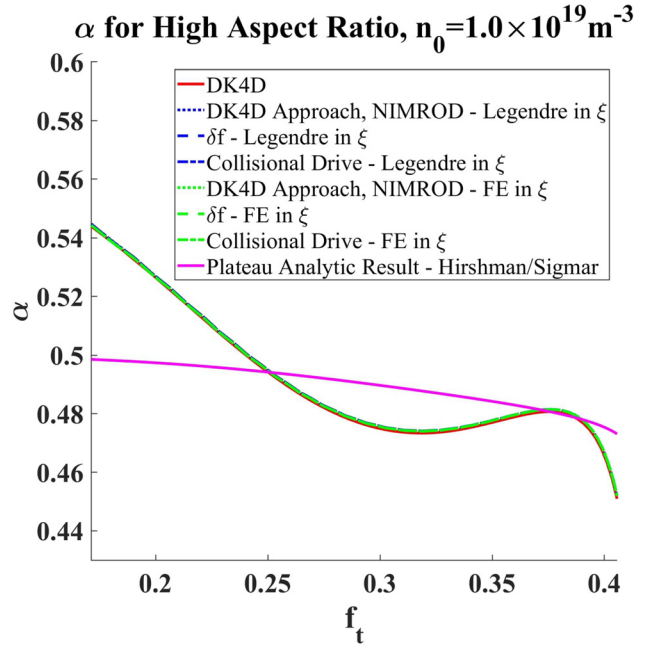

FIG. 6. α profiles for the high aspect ratio case with $\hat{\nu} \sim 1$ show excellent agreement between all of NIMROD's numerical approaches and DK4D. The analytic result shown is the plateau regime result from Hirshman and Sigmar.[22]

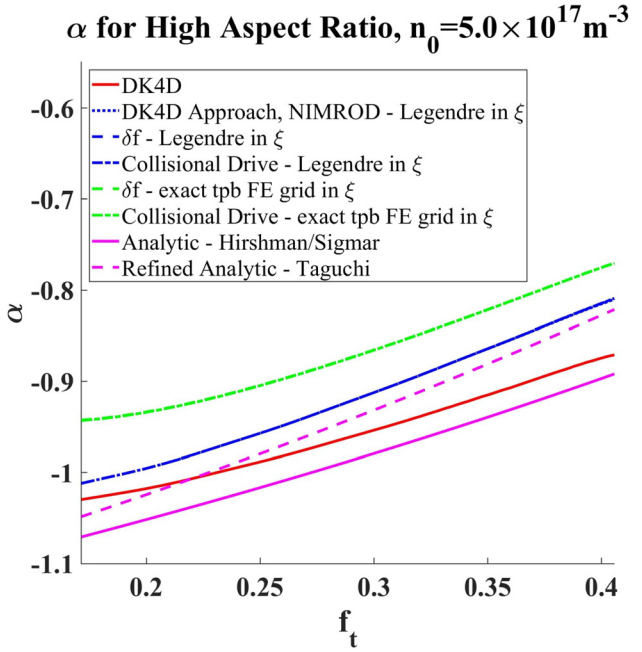

FIG. 7. α profiles for the high aspect ratio case with $\hat{\nu} \sim 10^{-4}$. Here, Legendre polynomial cases in NIMROD use a maximum degree of 57, as in DK4D. All NIMROD exact tpb FE curves (green) agree between each other, as well as all NIMROD Legendre curves (blue). Analytic (magenta) and DK4D (red) curves are also shown.

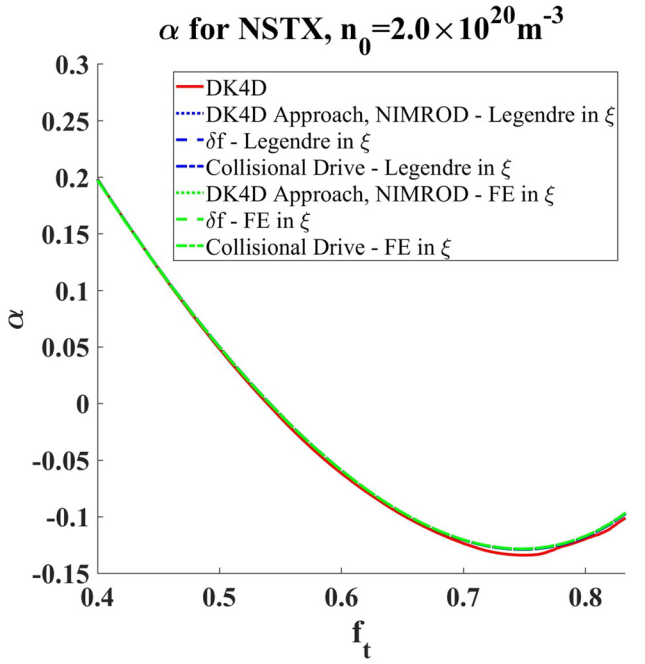

FIG. 8. α profiles for the NSTX case with $\hat{\nu} \sim 1$ show excellent agreement between all of NIMROD's numerical approaches and DK4D.

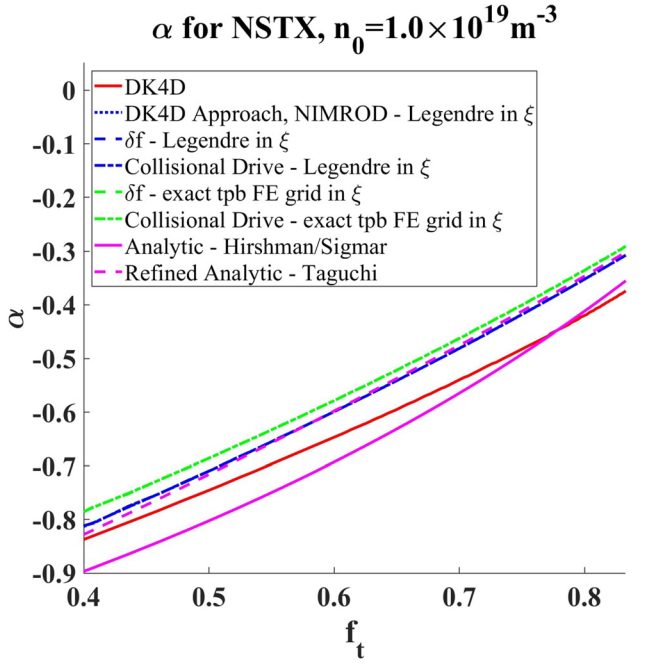

FIG. 9. α profiles for the NSTX case with $\hat{\nu} \sim 10^{-4}$. Here, Legendre polynomial cases in NIMROD use a maximum degree of 73, as in DK4D. All NIMROD exact tpb FE curves (green) agree between each other, as well as all NIMROD Legendre curves (blue). Analytic (magenta) and DK4D (red) curves are also shown.

term seems to be able to fix this problem; however, it modifies the solution in the low-collisionality, banana regime cases presented herein. We have preliminarily implemented and tested an *ad hoc* diffusion term for more relevant test cases that we will use in future work, with positive results so far; however, this is a work in progress.

For the banana regime collisionality results, the analytics are also seen to differ from the numerics both for NIMROD and DK4D. This disagreement is partly due to the fact that we are not completely in the deep banana regime. A $\hat{\nu} \sim 10^{-4}$ translates to $\nu^\star \sim 10^{-2}$ for the high aspect ratio case and $\nu^\star \sim 10^{-3}$ for the NSTX case. We have observed that a $\nu^\star$ of about 10^{-4} is required to be in the asymptotic regime where the analytics are valid. It is also noted that Taguchi's refined analytic result,[24] which goes to a higher Legendre expansion of the non-pitch-angle-scattering part of the collision operator, gives better agreement with our results than the Hirshman/Sigmar analytic formulation. This shows that getting the collision operator right in an analytic formulation is important, even in the banana regime where collisions at the tpb remain important.

For an additional comparison, we ran at $\nu^\star \sim 10^{-4}$ for both the high aspect ratio and NSTX equilibrium. We compare these results for α (where we use the exact tpb FE grid in ξ) to Taguchi's analytic formulation in Fig. 10. Here, we see that when using our converged results (both in resolution and $\nu^\star$) and Taguchi's refined analytic formula, the difference is reduced to less than 5%. This last discrepancy might well be resolved by refining the analytic formulation even further.

IX. CONCLUSIONS AND FUTURE WORK

As shown herein, we have successfully verified and benchmarked several NIMROD continuum kinetic formulations. We have compared the results for the poloidal flow coefficient α between the different NIMROD formulations, analytics, and DK4D in various collisionality regimes. Results agree very well between the approaches in the higher collisionality regime ($\hat{\nu} \sim 1$). In the banana collisionality regime ($\hat{\nu} \sim 10^{-4}$), the results differ. However, it was noted that the Legendre results are not converged in the banana regime, a familiar problem in banana regime drift kinetics. It is also seen that going to a refined analytic formulation for α—namely, using the Taguchi formula—further reduces the discrepancy between NIMROD's numerical results and analytics to less than 5%.

The agreement of results in the higher collisionality regime indicate the NIMROD's general implementation of the collision operator, which allows for several basis sets in 2D velocity space, most notably the exact FE tpb grids, is accurate and efficient. A description of the implementation and further verification may be found in Ref. 26.

Having verified the CEL-DKE solutions, further testing of the fluid/kinetic coupling of the CEL approach is warranted before pursuing relevant fusion-related questions using our continuum kinetic formulation. One immediate planned area of focus will be to use the CEL kinetic formulation in NIMROD to continue prior work on the effects of nonlinear mode penetration by RMPs in tokamaks.[15] This research was previously done in a slab geometry using NIMROD's fluid model and a heuristic closure for the viscous stress tensor. Current continuum kinetic capabilities would allow us to run in tokamak geometry using our more rigorous closure for the viscous stress tensor. Importantly, in the problem of time-dependent forced reconnection, the needed ion viscosity for the closure scheme must incorporate

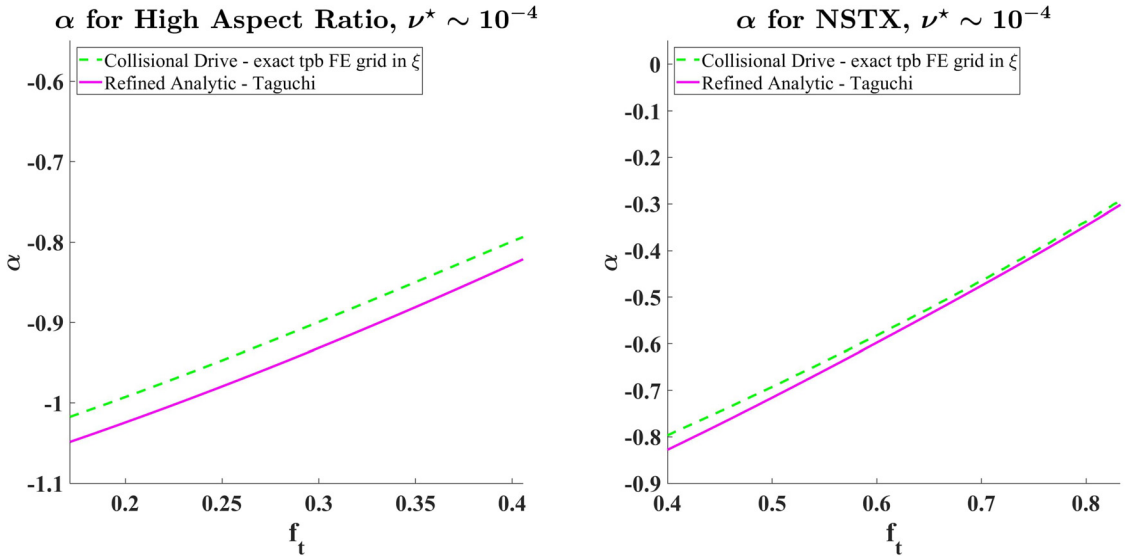

FIG. 10. Comparison of α profiles for $\nu^\star \sim 10^{-4}$, with the Taguchi[24] analytic formula. Here, we use an exact tpb FE grid in ξ with GLL polynomials, and the profiles agree within 5%.

temporal dependence.[28,37] Simplified viscosity models based on time-asymptotic neoclassical viscosity calculations cannot rigorously model these effects, but a fully coupled ion CEL-DKE/fluid model in NIMROD can.

Overall, our verification efforts for the continuum kinetic formulations in NIMROD have been a success, and we anticipate many future applications to plasma and fusion-related problems of interest.

ACKNOWLEDGMENTS

This research was supported by the U. S. Department of Energy (DOE) Office of Science, Office of Fusion Energy Science under Grant Nos. DE-FG02-86ER53218, DE-SC0018146, DE-SC0018109, and DE-AC02-05CH11231. This research used resources of the National Energy Research Scientific Computing Center (NERSC), a U.S. Department of Energy Office of Science User Facility located at Lawrence Berkeley National Laboratory.

APPENDIX: COLLISION OPERATOR SPECIFICS

For the simulations herein we use only the ion–ion portion of the full, linearized Fokker–Planck Coulomb collision operator. The ion–ion part is made up of a "test particle" term and a "field particle" term. The test particle part is given as

$$C(f_{i1},f_{Mi}) = \frac{\nu_{ii}}{2s^3}(\phi_{\rm err}(s)-\chi(s))\left\{\frac{\partial}{\partial\xi}\left((1-\xi^2)\frac{\partial f_{i1}}{\partial\xi}\right)\right\} + \frac{\nu_{ii}}{s^2}\frac{\partial}{\partial s}\left\{\chi(s)\left[s\frac{\partial f_{i1}}{\partial s}+2s^2 f_{i1}\right]\right\}, \tag{A1}$$

where $\chi(s) = (\phi_{\rm err}(s) - s\phi'_{\rm err}(s))/(2s^2)$ is the Chandrasekhar function, and

$$\nu_{ii} = \frac{n_i e^4 \ln(\Lambda_{ii})}{4\pi\epsilon_0^2 m_i^2 v_{Ti}^3}. \tag{A2}$$

The numerical evaluation of Eq. (A1) is straightforward and involves an integration by parts of the Lorentz term after multiplication by the test function in the Galerkin approach (see Ref. 16). The field particle part is given as

$$C(f_{Mi},f_{i1}) = \frac{e^4\ln(\Lambda_{ii})}{4\pi\epsilon_0^2 m_i^2}\left\{4\pi f_{i1} + \frac{2s^2}{v_{Ti}^4}\frac{\partial G_i}{\partial s^2} - \frac{2}{v_{Ti}^2}H_i\right\}f_{Mi}, \tag{A3}$$

where $G_i \equiv \int d^3\mathbf{v}' f_{i1}|\mathbf{v}-\mathbf{v}'|$ and $H_i \equiv \int d^3\mathbf{v}' f_{i1}|\mathbf{v}-\mathbf{v}'|^{-1}$ are the Rosenbluth potentials. The numerical evaluation of the Rosenbluth potential integrals is nontrivial. The accurate and efficient evaluation of Eq. (A3) is discussed in detail in Ref. 26.

We also note here that the exact definition of the Coulomb logarithm does make a significant difference when running in higher collisionality regimes. To be consistent with DK4D, we used the same definition, namely,

$$\ln(\Lambda_{ii}) = \ln\left(\frac{\sqrt{\epsilon_0 T_i/(n_i e^2)}}{e^2/(\pi\epsilon_0 m_i v_{Ti}^2)}\right), \tag{A4}$$

which differs from that in Ref. 23 by a factor of 2 inside the logarithm. Equation (A4) differs from the NRL plasma formulary definition,[39]

$$\ln(\Lambda_{ii}) = 23 - \ln\left[\frac{1}{T_i}\left(\frac{2\times10^{-6}n_i}{T_i}\right)^{(1/2)}\right], \tag{A5}$$

by as much as 7% for the higher collisionality ($\hat{\nu}\sim 1$) equilibria used herein. This led to ~5% or greater differences in our results for α. In Eq. (A5), T_i is measured in eV without an implied

Boltzmann factor multiplication, and n_i is measured in m^{-3}. Equation (A5) is more typically used in NIMROD continuum kinetic calculations.

DATA AVAILABILITY

The code used to produce the results contained in this study can be found in the Tech-X NIMROD repository at https://ice.txcorp.com/nimsvn/nimroot, Ref. 38. Input files that support the findings of this study are available from the corresponding author upon reasonable request.

REFERENCES

[1]W. X. Qu and J. D. Callen, "Nonlinear growth of a single neoclassical MHD tearing mode in a tokamak," Report No. UWPR 85-5 (University of Wisconsin, 1985).
[2]R. Carrera, R. D. Hazeltine, and M. Kotschenreuther, "Island bootstrap current modification of the nonlinear dynamics of the tearing mode," Phys. Fluids **29**, 899–902 (1986).
[3]J. D. Callen, W. X. Qu, K. D. Siebert, B. A. Carreras, K. C. Shaing, and D. A. Spong, *Neoclassical MHD Equations, Instabilities and Transport in Tokamaks* (IAEA, 1987).
[4]C. C. Hegna, "The physics of neoclassical magnetohydrodynamic tearing modes," Phys. Plasmas **5**, 1767–1774 (1998).
[5]R. J. Buttery, S. Günter, G. Giruzzi, T. C. Hender, D. Howell, G. Huysmans, R. J. L. Haye, M. Maraschek, H. Reimerdes, O. Sauter, C. D. Warrick, H. R. Wilson, and H. Zohm, "Neoclassical tearing modes," Plasma Phys. Controlled Fusion **42**, B61–B73 (2000).
[6]O. Sauter, E. Westerhof, M. L. Mayoral, B. Alper, P. A. Belo, R. J. Buttery, A. Gondhalekar, T. Hellsten, T. C. Hender, D. F. Howell, T. Johnson, P. Lamalle, M. J. Mantsinen, F. Milani, M. F. F. Nave, F. Nguyen, A. L. Pecquet, S. D. Pinches, S. Podda, and J. Rapp, "Control of neoclassical tearing modes by sawtooth control," Phys. Rev. Lett. **88**, 105001 (2002).
[7]R. J. La Haye, "Neoclassical tearing modes and their control," Phys. Plasmas **13**, 055501 (2006).
[8]J. W. Berkery, S. A. Sabbagh, R. E. Bell, S. P. Gerhardt, and B. P. LeBlanc, "A reduced resistive wall mode kinetic stability model for disruption forecasting," Phys. Plasmas **24**, 056103 (2017).
[9]Y. Liu, M. S. Chu, I. T. Chapman, and T. C. Hender, "Toroidal self-consistent modeling of drift kinetic effects on the resistive wall mode," Phys. Plasmas **15**, 112503 (2008).
[10]J. W. Berkery, S. A. Sabbagh, R. Betti, B. Hu, R. E. Bell, S. P. Gerhardt, J. Manickam, and K. Tritz, "Resistive wall mode instability at intermediate plasma rotation," Phys. Rev. Lett. **104**, 035003 (2010).
[11]G. Xia, Y. Liu, L. Li, C. Ham, Z. Wang, and S. Wang, "Effects of poloidal and parallel flows on resistive wall mode instability in toroidally rotating plasmas," Nucl. Fusion **59**, 126035 (2019).
[12]N. Aiba, J. Shiraishi, and S. Tokuda, "Impact of plasma poloidal rotation on resistive wall mode instability in toroidally rotating plasmas," Phys. Plasmas **18**, 022503 (2011).
[13]R. Fitzpatrick, "Interaction of tearing modes with external structures in cylindrical geometry (plasma)," Nucl. Fusion **33**, 1049–1084 (1993).
[14]M. T. Beidler, J. D. Callen, C. C. Hegna, and C. R. Sovinec, "Nonlinear modeling of forced magnetic reconnection in slab geometry with nimrod," Phys. Plasmas **24**, 052508 (2017); see also Erratum **25**, 049901 (2018).
[15]M. T. Beidler, J. D. Callen, C. C. Hegna, and C. R. Sovinec, "Mode penetration induced by transient magnetic perturbations," Phys. Plasmas **25**, 082507 (2018).
[16]E. D. Held, S. E. Kruger, J.-Y. Ji, E. A. Belli, and B. C. Lyons, "Verification of continuum drift kinetic equation solvers in NIMROD," Phys. Plasmas **22**, 032511 (2015).
[17]B. C. Lyons, "Steady-state benchmarks of DK4D: A time-dependent, axisymmetric drift-kinetic equation solver," Phys. Plasmas **22**, 056103 (2015).
[18]R. D. Hazeltine and J. D. Meiss, *Plasma Confinement* (Dover, Mineola, NY, 2003).
[19]J. J. Ramos, "Fluid and drift-kinetic description of a magnetized plasma with low collisionality and slow dynamics orderings. i. electron theory," Phys. Plasmas **17**, 082502 (2010).
[20]K. C. Shaing and D. A. Spong, "Extending the collisional fluid equations into the long mean-free-path regime in toroidal plasmas. i. plasma viscosity," Phys. Fluids B **2**, 1190–1194 (1990).
[21]J. P. Wang and J. D. Callen, "Fluid/kinetic hybrid moment description of plasmas via a Chapman–Enskog-like approach," Phys. Fluids B **4**, 1139–1151 (1992).
[22]S. P. Hirshman and D. J. Sigmar, "Neoclassical transport of impurities in tokamak plasmas," Nucl. Fusion **21**, 1079 (1981).
[23]P. Helander and D. J. Sigmar, *Collisional Transport in Magnetized Plasmas* (Cambridge University Press, New York, 2002).
[24]M. Taguchi, "Analytic expression for poloidal flow velocity in the banana regime," Phys. Plasmas **20**, 014505 (2013).
[25]G. F. Chew, M. L. Goldberger, and F. E. Low, "The Boltzmann equation and the one-fluid hydromagnetic equations in the absence of particle collisions," Proc. R. Soc. London, Ser. A **236**, 112–118 (1956).
[26]J. A. Spencer, B. Adair, E. D. Held, J.-Y. Ji, and J. R. Jepson, "Accurate numerical, integral methods for computing drift-kinetic Trubnikov-Rosenbluth potentials," J. Comput. Phys. (submitted) (2021).
[27]R. C. Morris, Ph.D. dissertation (Imperial College of Science, Technology and Medicine, 1995).
[28]R. C. Morris, M. G. Haines, and R. J. Hastie, "The neoclassical theory of poloidal flow damping in a tokamak," Phys. Plasmas **3**, 4513–4520 (1996).
[29]J. J. Ramos, "Fluid and drift-kinetic description of a magnetized plasma with low collisionality and slow dynamics orderings. II. Ion theory," Phys. Plasmas **18**, 102506 (2011).
[30]J. DeLucia, S. Jardin, and A. Todd, "An iterative metric method for solving the inverse tokamak equilibrium problem," J. Comput. Phys. **37**, 183–204 (1980).
[31]C. Sovinec, A. Glasser, T. Gianakon, D. Barnes, R. Nebel, S. Kruger, S. Plimpton, A. Tarditi, M. Chu, and N. T. the, "Nonlinear magnetohydrodynamics with high-order finite elements," J. Comput. Phys. **195**, 355 (2004).
[32]M. Landreman and D. R. Ernst, "New velocity-space discretization for continuum kinetic calculations and Fokker-Planck collisions," J. Comput. Phys. **243**, 130–150 (2013).
[33]E. A. Belli and J. Candy, "Kinetic calculation of neoclassical transport including self-consistent electron and impurity dynamics," Plasma Phys. Controlled Fusion **50**, 095010 (2008).
[34]R. W. Harvey and M. G. McCoy, "The CQL3D Fokker-Planck code," in *IAEA TCM on Advances in Simulation and Modeling of Thermonuclear Plasmas* (IAEA, Montreal, Canada, 1992), pp. 489–526, available through USDOC/NTIS No. DE93002962.
[35]J. Candy and R. Waltz, "An Eulerian gyrokinetic-Maxwell solver," J. Comput. Phys. **186**, 545–581 (2003).
[36]M. Barnes, W. Dorland, and T. Tatsuno, "Resolving velocity space dynamics in continuum gyrokinetics," Phys. Plasmas **17**, 032106 (2010).
[37]A. L. Garcia-Perciante, J. D. Callen, K. C. Shaing, and C. C. Hegna, "Time-dependent neoclassical viscosity," Phys. Plasmas **12**, 052516 (2005).
[38]See https://ice.txcorp.com/nimsvn/nimroot for "Tech-X NIMROD Repository, branch: Cel_neo, svn version number: 7407" (2021).
[39]A. S. Richardson, *NRL Plasma Formulary* (Naval Research Laboratory, 2019).